

# Infrared Glass–Ceramics with Multidispersion and Gradient Refractive Index Attributes

Laura Sisken, Myungkoo Kang, Johann M. Veras, Charmayne Lonergan, Andrew Buff, Anupama Yadav, Devon McClane, Cesar Blanco, Clara Rivero-Baleine, Theresa S. Mayer, and Kathleen A. Richardson\*

Infrared (IR) glass–ceramics (GCs) hold the potential to dramatically expand the range of optical material solutions available for use in bulk and planar optical systems in the IR. Current material solutions are limited to single- or polycrystalline materials and traditional IR-transparent optical glasses. GCs that can be processed with spatial control and extent of induced crystallization present the opportunity to realize an effective refractive index variation, enabling arbitrary gradient refractive index elements with tailored optical function. This work discusses the role of the parent glass composition and morphology on nanocrystal phase formation in a multicomponent chalcogenide glass. Through a two-step heat treatment protocol, a Ge–As–Pb–Se glass is converted to an optical nanocomposite where the type, volume fraction, and refractive index of the precipitated crystalline phase(s) define the resulting nanocomposite's optical properties. This modification results in a giant variation in infrared Abbe number, the magnitude of which can be tuned with control of crystal phase formation. The impact of these attributes on the GCs' refractive index, transmission, dispersion, and thermo-optic coefficient is discussed. A systematic protocol for engineering homogeneous or gradient changes in optical function is presented and validated through experimental demonstration employing this understanding.

## 1. Introduction

Infrared (IR) optical systems are increasingly employed in nondefense applications including commercial IR cameras,<sup>[1]</sup> automotive sensors,<sup>[2]</sup> defect detection in manufacturing,<sup>[3]</sup> in the medical field,<sup>[4]</sup> and in a range of other chemical/biological applications. A key reason for this increased use correlates with the decrease in price of the components needed to build these systems, combined with an increase in the availability of components. Such IR systems have traditionally been made of crystalline optical components, based on materials which can be costly to grow and subsequently manufacture into parts. Chalcogenide glass (ChG) optical elements can be less expensive to process, can be compositionally tailored toward specific optical properties, and are readily fabricated into their desired form via manufacturing processes such as precision glass molding or single point diamond turning.<sup>[5,6]</sup> Another way to further reduce the cost of these systems without degrading their performance is to add


optical functionality to the individual components through the creation of gradient refractive index (GRIN) profiles within the components. GRIN components offer the opportunity to reduce the size, weight, and/or number of optical elements needed in an optical system while still maintaining or improving the system's optical performance.<sup>[7]</sup>

Multiple methods have been explored to realize GRIN optical elements in the IR (as summarized in a recent review<sup>[8]</sup>) including stacking and pressing of glass layers,<sup>[9–11]</sup> chemical vapor deposition,<sup>[12]</sup> metamaterials,<sup>[13]</sup> and lithographic laser patterning processes.<sup>[14]</sup> Recently, GRIN structures have been demonstrated in IR optical glasses employing techniques using solution processing to direct write/print multilayer structures,<sup>[8,15]</sup> and through gradients of nanorods of IR glasses with differing refractive indices.<sup>[16]</sup> In addition, laser-induced crystallization and/or vitrification has recently been shown to enable spatial control of refractive index within a single, homogeneous material.<sup>[8,17,18]</sup> Recently, it has also been shown that through the use of micropoling, one can induce local compositional

Dr. L. Sisken, Dr. M. Kang, Dr. C. Lonergan, A. Buff, Dr. A. Yadav, D. McClane, C. Blanco, Prof. K. A. Richardson  
CREOL, College of Optics and Photonics  
University of Central Florida  
Orlando, FL 32816, USA  
E-mail: kcr@creol.ucf.edu

Dr. J. M. Veras, Dr. C. Rivero-Baleine  
Missiles and Fire Control  
Lockheed Martin Corporation  
Orlando, FL 32819, USA

Prof. T. S. Mayer<sup>[†]</sup>  
Department of Electrical Engineering  
Pennsylvania State University  
University Park  
PA 16802, USA

 The ORCID identification number(s) for the author(s) of this article can be found under <https://doi.org/10.1002/adfm.201902217>.

<sup>[†]</sup>Present address: Department of Electrical and Computer Engineering, Virginia Tech, Blacksburg, VA 24060, USA

DOI: 10.1002/adfm.201902217

variation through a patterned electrode thereby modifying both local refractive index<sup>[8,19,20]</sup> and the glass' nonlinear optical properties resulting in spatially defined second harmonic generation.<sup>[8,21]</sup>

A strategy explored in the present effort is a first step in creating GRIN elements through spatial control of the formation of secondary crystalline phase(s) to form an optical glass–ceramic (GC) or nanocomposite in the GeSe<sub>2</sub>–As<sub>2</sub>Se<sub>3</sub>–PbSe (GAP-Se) glass system. Demonstrated for a range of compositions suitable for use in the IR, this paper explores the role of as-formed glass composition and morphology on resulting postheat treatment microstructure. The specific heat treatment process chosen to induce this microstructure can vary, and the actual time duration and temperature choice of the heat treatment will locally vary the volume fraction (and type) of nanocrystals within the parent ChG matrix. The resulting nanocrystal-containing glass formed is an optical nanocomposite, and spatial variation of this nanocrystal distribution can thereby create an effective refractive index gradient. Such an approach has been recently employed to demonstrate this strategy forming a focusing optic.<sup>[22]</sup> In order to maintain low optical loss, the number density, type, and size of the crystallites must remain small. Additionally, the crystal phase formed must possess low absorption loss in the spectral region of interest. The shape and magnitude of the refractive index gradient are defined by the number density of the nanocrystallite phase(s) formed, as well as their shape, size, refractive index, and spatial position within the parent glass. By locally controlling the relative volume fraction of crystal and glass phases, the gradient can be established. This strategy to form a GRIN enables creation of a 3D, arbitrary GRIN profile (full spatial control of index in the *x*-, *y*-, and *z*-directions). Such a profile can be spatially controlled by employing a focused laser to initiate nucleation (a precursor to crystallite growth) and/or growth of crystalline nuclei to realize

a desired “filling fraction” within a now compositionally modified, lower refractive index base glass matrix. Design of the desired index profile requires an understanding of the glass science (parent glass nucleation and growth kinetics), the preferential nature of crystallization of specific precipitating phases, the resulting change in the base glass (now depleted of crystal forming constituents), and the corresponding impact of these variables on the resulting optical properties of the nanocomposite GC. While complex in terms of variables, these options provide a broad range of realizable attributes within a single parent glass system subjected to a variety of processing (nucleation plus growth) conditions.

## 2. Results and Discussion

Such a GRIN nanocomposite is depicted schematically in **Figure 1a**, where the parent glass matrix has a lower refractive index than that of nanocrystals formed through thermal nucleation and growth protocols. In addition to generating changes in optical properties, the postheat-treated GC also exhibits changes in other properties such as glass transition temperature, Vickers microhardness, density, and thermal properties as discussed in detail elsewhere.<sup>[23]</sup> This multiphase, nanocomposite approach has been demonstrated in thin films of the same GAP-Se glass compositions examined here.<sup>[17]</sup> The GAP-Se glass system has been shown to exhibit a wide range of glass-forming abilities as shown in **Figure 1b**<sup>[24]</sup> where the authors evaluated the ability of select compositions of glasses to form GCs upon thermal heat treatment but did not consider the possibility of spatially varying the location and/or concentration of the precipitated phase within the glass matrix or the effects of the crystalline phases on optical properties other than transmission. In the present study, the aim has been to

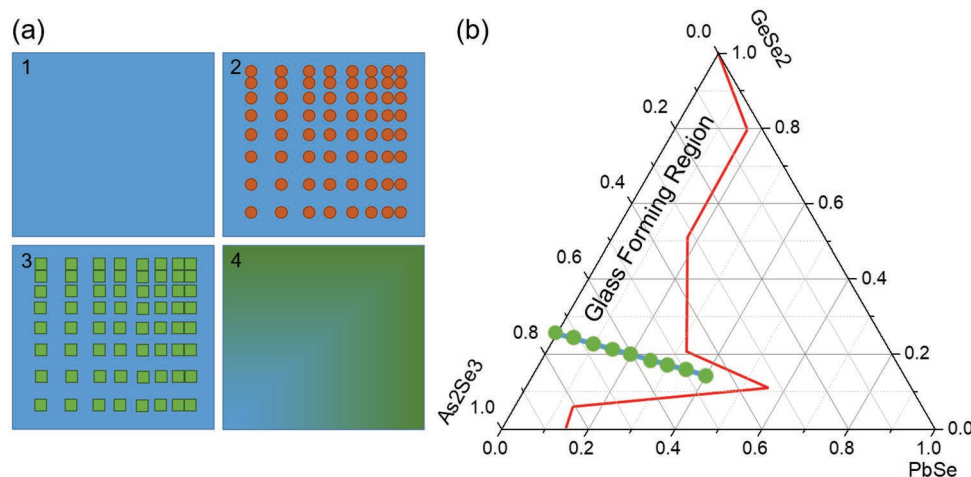


**Figure 1.** a) A schematic of a ChG-based optical nanocomposite GRIN element formed from 1) a crystal-free base glass; 2) glass with spatially dispersed nuclei (red circles) with a graded concentration profile; 3) conversion of nuclei with a further (growth) heat treatment to yield crystals (green squares) at the sites of prior nucleation (only) and not in areas that were not prenucleated; this variation in number density of high-index nanocrystals within a low-index parent glass matrix results in 4) an effective refractive index variation directly proportional to the local variation in the volume fraction of crystals and the refractive indices of the crystalline phases present. b) The glass-forming region of the GeSe<sub>2</sub>–As<sub>2</sub>Se<sub>3</sub>–PbSe ternary as originally investigated by Yang et al.<sup>[24]</sup> and those compositions (green circles) investigated in this study. The region to the left of the red line defines the glass forming region whereas glasses to the right of this line crystallize. The compositions along the green dots represent the tie line of base glasses with a constant GeSe<sub>2</sub>:3As<sub>2</sub>Se<sub>3</sub> ratio with additions of PbSe ranging from 0 to 40 mol%.

evaluate how the amount of PbSe in the parent glass impacts the starting glass' morphology and optical properties, and affects the crystal phase formation upon heat treatment. The resulting GC's microstructure defines the optical properties of the nanocomposite and is directly related to these variables. The tie line defined by a line connecting the green dots shown in Figure 1b illustrates the compositional space investigated in the present study, where laboratory prepared melt-quenched base glasses of constant  $\text{GeSe}_2\text{:}3\text{As}_2\text{Se}_3$  ratio with additions of PbSe (ranging from 0–40 mol%) were prepared. As previously noted, these GAP-Se base glasses exhibit a systematic variation in thermomechanical and other physical properties with PbSe addition as reported for bulk glasses<sup>[25]</sup> and can be used to form ultralow dispersion GRIN optics as demonstrated in films.<sup>[17]</sup> Glasses within the same system have served as a basis for demonstration of a 3D GRIN structure,<sup>[22]</sup> and can be scaled from laboratory to commercial scale demonstrating the manufacturability of low-loss GRIN materials suitable for the mid-wave IR (MWIR).<sup>[23,26]</sup>

As pertinent background to the present study, within the composition space of traditional melt-derived glasses ranging from 0 to 55 mol% PbSe (0–17.6 at% Pb), the resulting glasses, while amorphous, exhibit liquid–liquid phase separation (LLPS) consisting of Pb-rich and Pb-deficient glass phases.<sup>[25]</sup> A broad immiscibility dome seen across the glass-forming region (between  $\approx 10$  and 45 mol% PbSe) of the studied tie line has been shown to have a direct impact on the composition of the precipitated crystal phase and that of the residual glass matrix in the postcrystallized GC.<sup>[24,27]</sup> It should be noted that in a similar nonstoichiometric composition made from the same elemental starting materials,  $(\text{Ge}_{30}\text{As}_{10}\text{Se}_{60})_{1-x}\text{PbSe}_x$ , extensive phase separation was also reported, which suggests that phase separation may be common to compositions containing these elements.<sup>[28–30]</sup> As quantified by thermal analysis and differential scanning calorimetry (DSC) measurements, increasing Pb content leads to a lowering of the glass' stability, enhancing the likelihood of devitrification.<sup>[23]</sup> Thus, in the case of a glass with a droplet/matrix morphology, it is likely that the Pb-rich glass phase will be where crystallization occurs first. Additionally, the boundaries between the dissimilar glassy phases may also serve as heterogeneous nucleation sites, though crystallization has not been explicitly observed at this interface, in the present effort.<sup>[23]</sup>

Due to the nonhomogeneous nature of the parent glasses at high PbSe levels, a further description of the starting glass morphology examined here is warranted, as this morphology will define the postheat-treated GCs microstructure and as will be shown, the evolution of novel optical properties. As previously reported<sup>[25,31,32]</sup> and noted above, the base glass morphology across the  $(\text{GeSe}_2\text{--}3\text{As}_2\text{Se}_3)_{1-x}\text{PbSe}_x$  series exhibits liquid–liquid phase separation, and glasses within the midrange of compositions ( $x \approx 10\text{--}40$  mol% PbSe) are dominated by metastable phase separation (droplet/matrix morphology) with a narrow range of unstable (spinodal decomposition) morphology.<sup>[23]</sup> This behavior will ultimately influence the probability of successful conversion from glass to a low-optical-loss GC, and the magnitude of postheat-treated physical property change. Shown explicitly in this study, we confirm that the dominant crystalline phases formed and the composite's refractive index

are dictated by the low-stability Pb-rich phase within the parent glass as characterized by a lower  $\Delta T$  (where  $\Delta T = T_x - T_g$ ), where  $T_x$  and  $T_g$  correspond to the glass' crystallization temperature and transition temperature, respectively (see the Supporting Information). With increasing Pb content across the GAP-Se series, variations in material morphology (both droplet size and Pb content of the droplet or matrix) occur in the Pb-rich phase. Both of these attributes influence the type and number of crystalline phases formed upon heat treatment. The size of the droplet phase for the series examined here varies with Pb-content despite all glasses having the same melt size and thermal (melt/quench) history. Over the range of compositions of interest here, the size of the Pb-rich droplets increases as they are first observed (near  $\approx 10$  mol% PbSe) and as the PbSe content approaches  $\approx 25\text{--}30$  mol%. Following a small region of spinodal decomposition between 30 and 35 mol%, the material then exhibits a droplet/matrix morphology comprised of Pb-deficient droplets in a Pb-rich matrix, where droplet size decreases with increasing PbSe. These regions of morphological transition ( $\approx 10$  mol% PbSe: transition from a homogeneous glass to a phase-separated material, 25%: transition from Pb-rich droplet to spinodal, 35%: transition to Pb-deficient droplets) would be compositional thresholds where transitions in pre- and postheat treatment optical property trends would likely occur and be expected to be most pronounced. Such observations are specifically reported in the findings below. This background provides context as to how the GC microstructure resulting from the nucleation and growth protocols used in this study is directly correlated to starting glass morphology as well as resulting changes in postheat-treated optical properties.

Discussed herein are comparisons of pre- and postheat-treated optical properties for  $(\text{GeSe}_2\text{--}3\text{As}_2\text{Se}_3)_{1-x}\text{PbSe}_x$  glasses prepared with  $x = 0\text{--}40$  mol% in 5 mol% increments. In all cases, glasses were nucleated at their  $T_g$ , and then grown at the temperature corresponding to the peak ( $T_p$ ) of the first crystallization exotherm as observed by DSC. As heat treatment of the base glass gives rise to changes in the optical properties of the resulting GC, the magnitude and sign of these changes were quantified with composition and related starting morphology to assess the role of ceramization on the resulting nanocomposite's optical properties. The type and volume fraction of crystal species in the resulting GC were examined to see if the optical changes were attributable to structural re-arrangement or crystallization. Additionally, the crystal phase identity, refractive index, and volume fraction were used to model and interpret the resulting nanocomposite's effective refractive index. The correlation in changes of optical properties upon this "fixed" nucleation and growth protocol (determined from prior measurements of nucleation- and growth-like curves for these glasses<sup>[23]</sup>) has been compared to evaluate trends in postprocessed GCs that would guide design inputs required for optical system design by defining end points of (property) change for these materials. Key thermal properties of glasses used for determination of nucleation and growth curves are included in the Supporting Information.

X-ray diffraction (XRD) was used to verify that the parent, as-melted base glasses were amorphous and to determine the type and volume fraction of the various crystal phases present

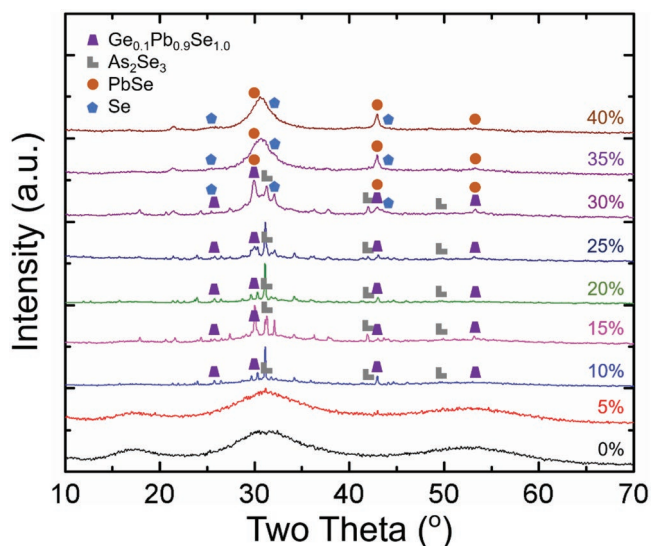


**Figure 2.** XRD spectra of the postheat-treated samples for the compositional series where PbSe content varies from 5 to 40 mol% PbSe. The  $x = 0$  mol% PbSe spectrum was added as a reference for the Pb-free Ge–As–Se base glass. Crystal phase identities for peaks shown are indicated by the symbols corresponding to  $\text{Ge}_{0.1}\text{Pb}_{0.9}\text{Se}_{1.0}$ ,  $\text{As}_2\text{Se}_3$ , PbSe, and Se.

in the nucleated [N] and grown [G] samples. An explanation of how we calibrated volume fractions and considered Pb in residual glass not participating in crystallization for the XRD data is discussed in the “Experimental Section.” The XRD spectra of the nucleated and grown [N+G] samples are shown in **Figure 2** where the type of crystal phases formed is identified and defined in the legend. The type and volume fraction of each crystal phase identified from XRD data are summarized in **Table 1**. The 0 mol% PbSe (Pb-free) glass sample did not have heat treatment performed on it as the material did not exhibit a crystallization exotherm; however, its XRD spectrum was added as a representative indication of the Pb-free Ge–As–Se network for the base glass. As can be seen, the position of this amorphous hump associated with the glass’ network did not change significantly across the Pb-series’ composition range confirming that the PbSe addition does little to modify the glass’

**Table 1.** The volume fractions ( $V_x$ ) of each crystal phase present in the post-heat-treated glass–ceramic as determined via XRD as a function of PbSe content.

PbSe mol%	$V_x \text{Ge}_{0.1}\text{Pb}_{0.9}\text{Se}_{1.0}$ [%]	$V_x \text{As}_2\text{Se}_3$ [%]	$V_x \text{PbSe}$ [%]	$V_x \text{Se}$ [%]	Total $V_x$ crystal [%]	Total $V_g$ glass [%]
0%	≈0	≈0	≈0	≈0	≈0	100
5%	≈0	≈0	≈0	≈0	≈0	100
10%	3.26	16.82	≈0	≈0	20.08	79.92
15%	4.22	12.35	≈0	≈0	16.57	83.43
20%	5.44	13.36	≈0	≈0	18.80	81.20
25%	5.76	11.31	≈0	≈0	17.06	82.94
30%	≈0	11.68	5.94	2.92	20.53	79.47
35%	≈0	13.46	9.52	3.37	26.35	73.65
40%	≈0	14.07	10.45	3.52	28.04	71.96

backbone. The 5 mol% PbSe glass remained amorphous upon heat treatment, which is likely due to the relative stability of the parent glass phase ( $\Delta T = 150$  °C) and the lack of any evidence of liquid–liquid phase separation or presence of a segregated Pb-rich phase in the base glass. This suggests that the 5–10 mol% PbSe level represents a lower boundary of Pb concentration in the matrix where glass stability is retained upon heat treatment in the material as the heat treatment protocol used here shows no evidence of crystal phase formation. That said, other heat treatment protocols not examined in the present study for longer times or for the same time at higher temperatures may show crystal formation. A distinct change in the XRD spectra from 10 to 35 mol% PbSe can be observed. For compositions between 10 and 30 mol% PbSe, the primary crystal phases identified following heat treatment were  $\text{Ge}_{0.1}\text{Pb}_{0.9}\text{Se}_{1.0}$  and  $\text{As}_2\text{Se}_3$ , and as the amount of Pb was increased further, the volume fraction of the  $\text{Ge}_{0.1}\text{Pb}_{0.9}\text{Se}_{1.0}$  crystal was seen to increase with minimal change in the volume fraction of the  $\text{As}_2\text{Se}_3$  crystal. At a level of 35 mol% PbSe (within the spinodal decomposition region), a transition of crystal phases formed was observed. Here,  $\text{Ge}_{0.1}\text{Pb}_{0.9}\text{Se}_{1.0}$  crystals were no longer observed in the glass–ceramic. Meanwhile, PbSe and Se crystals emerged while the  $\text{As}_2\text{Se}_3$  remained present. The large changes in composition that are observed in the low PbSe glasses are likely due to the concentration of Pb in the amorphous droplet phase changing significantly as the amount of PbSe is increased up to the region of spinodal decomposition where the glass’ morphology changes from distinct droplets to a more “sponge-like” interconnected two-phase network with a more gradual transition between dissimilar compositional regions.<sup>[25]</sup>

Within the spinodal region which extends between ≈25 and 35 mol% PbSe, a clear change in the glass–ceramic’s postheat-treated microstructure is seen. Here new peaks for the high-index binary PbSe crystals as well as a small peak for Se are observed. This transition is consistent with previously reported X-ray energy dispersive spectroscopy (XEDS) data which showed no Pb-dominant droplet/matrix phase present; rather, a truly interconnected glass morphology comprised of regions of Pb-rich and Pb-deficient phases (with corresponding variation in the other glass’ constituents) co-exists with gradual compositional boundaries.<sup>[25]</sup> Beyond this region (i.e., at higher levels of 35 and 40 mol% PbSe), XRD patterns exhibit crystal phase content dominated by the Pb-rich matrix phase.

Here, the ternary  $\text{Ge}_{0.1}\text{Pb}_{0.9}\text{Se}_{1.0}$  crystal is no longer observed, replaced by the cubic binary PbSe crystals initially appearing as part of a broad peak in the 30 mol% PbSe spectrum near  $2\theta \approx 30^\circ$  and  $44^\circ$ . Also emerging in this higher PbSe region is the signature for Se crystals. These features confirm crystallization marked by a change in the region of Pb segregation. While still exhibiting droplet/matrix morphology at the higher levels of 35 and 40 mol% PbSe, Pb is now dominant in the matrix of the parent glass with much lower concentrations of Pb found in the Pb-deficient droplets. A concurrent change is seen in the other primary crystalline phase within the higher Pb GCs, specifically for

$\text{As}_2\text{Se}_3$ , where the volume fraction of these crystals is seen to decrease slightly across the 30–40 mol% PbSe composition range. Beyond this level, the ratio of all three crystals (PbSe, Se, and  $\text{As}_2\text{Se}_3$ ) remained essentially constant in the 35 and 40 mol% PbSe glasses, with a concurrent increase in the total volume fraction of all crystals as PbSe mol% increases. This phase evolution is consistent with our interpretation that additional Pb into the already Pb-rich matrix provides both Pb and Se needed to precipitate each as crystalline phases, with a concurrent reduction of these species in the residual glassy phase. Such variation, as described in the following sections, allows us to interpret both the contributions to the effective refractive index and dispersion behavior of the GC and the optical transmission which is impacted by the presence of both isotropic (PbSe) and anisotropic (Se,  $\text{As}_2\text{Se}_3$ ) precipitated phases.

Postheat treatment microstructure was investigated on select compositions in order to determine the type and morphology of crystals that formed and the impact of the precipitated crystals on both the nanocomposite's refractive index and dispersion change and its transmission loss/scattering. Since parent base glasses with 20 and 40 mol% PbSe possess two distinct, inverse starting morphologies,<sup>[23,25,31]</sup> transmission electron microscopy (TEM) images were collected from post-heat-treated samples of the two compositions along with corresponding XEDS images and selected area electron diffraction (SAED) patterns, to examine the resulting GC's nanoscale microstructure across this composition space. **Figure 3a** shows a dark field (DF) TEM image collected from a GC with 20 mol% PbSe where highly asymmetric, bright particles are distributed in a dark matrix. The contrast in brightness between the particles and the matrix

indicates that the atomic percentage of heavy elements in the particles is greater than that in the matrix. XEDS element maps shown in Figure 3b–e clearly indicate that the distribution of Pb, the heaviest element in the glass, matches that of the bright particles while other constituents have relatively uniform spatial distribution. Figure 3f shows a corresponding SAED pattern where spots corresponding to the two crystalline phases of  $\text{Ge}_{0.1}\text{Pb}_{0.9}\text{Se}_{1.0}$  and  $\text{As}_2\text{Se}_3$  are clearly evident, along with diffuse rings corresponding to an amorphous matrix. For the GC formed from the glass with 40 mol% PbSe, asymmetric, bright phases are interconnected, forming a matrix while dark phases are surrounded by the bright network phase, illustrative of particles, as shown in Figure 3g. XEDS element maps indicate that the distribution of Pb in this case matches that of the bright matrix while other constituents have similarly uniform spatial distribution, as shown in Figure 3h–k. Figure 3l shows a SAED pattern which includes spots corresponding to three crystalline phases of PbSe,  $\text{As}_2\text{Se}_3$ , and Se, along with diffuse rings corresponding to an amorphous matrix. The TEM data presented here confirm that i) the co-existence of Pb-rich and Pb-deficient phases in the starting parent glasses is maintained throughout heat treatment; ii) the Pb-rich phases are exclusively crystallized upon heat treatment; and iii) the types of crystalline phases identified are consistent with those seen in XRD data. As discussed in subsequent sections, such microstructural variation contributes to both the absorption and scatter loss seen in the change in transmissive properties of the glass–ceramic and the position of the short-wave transmission cut-off as well as other important optical properties of the resulting composite.

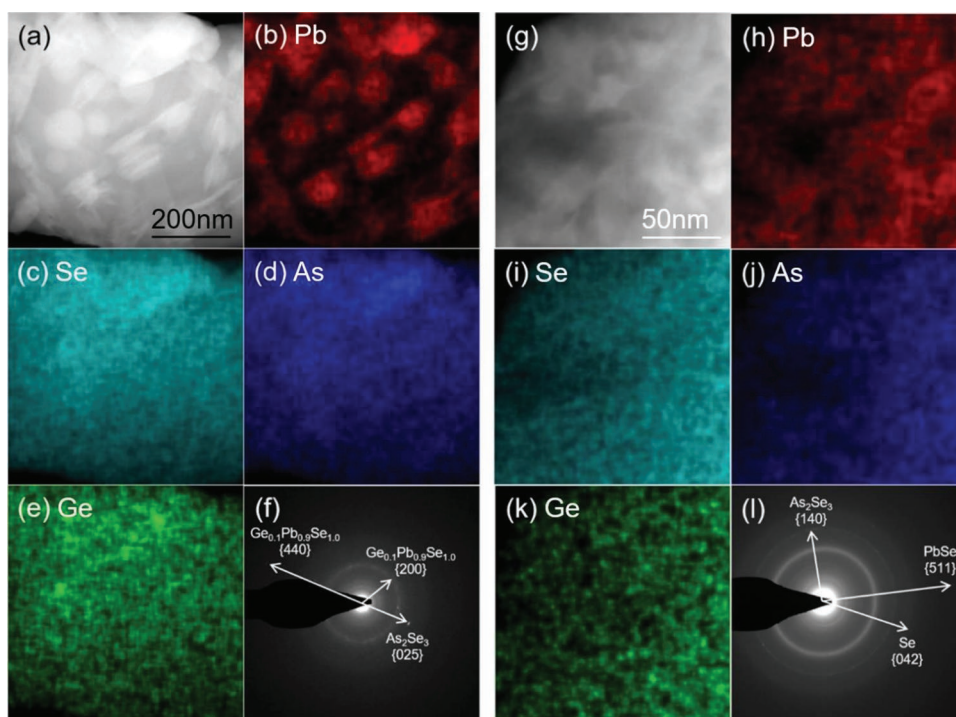


**Figure 3.** a) A DF TEM image collected from a post-heat-treated sample with 20 mol% PbSe along with XEDS element maps of b) Pb, c) Se, d) As, e) Ge, and f) the corresponding SAED pattern. g) A DF TEM image collected from a post-heat-treated sample with 40 mol% PbSe along with XEDS element maps of h) Pb, i) Se, j) As, and k) Ge and l) a corresponding SAED pattern.

As the primary application of the GAP-Se optical nanocomposite developed here has been for use in the MWIR, the refractive index for the base GAP-Se glasses and GC materials was measured in the MWIR (at  $\lambda = 4.515 \mu\text{m}$ ) at  $30^\circ\text{C}$ . Index data are shown as a function of parent glass PbSe (mol%) content in Figure 4a. For the base glass, one can observe a monotonic, though slightly exponential, increase in refractive index with an increase of Pb content in the glass. This can be correlated directly to the increasing content of the highly polarizable Pb species. What is interesting is the fact that the broad variation in morphology (homogeneous glass, droplet/matrix, or spinodal phase separation) across the series is not reflected in the glass' index behavior as compared to the delineation at these boundaries seen in other optical and physical properties of the parent glass.<sup>[20]</sup> However, the spatial position of the Pb defined by the glass morphology does impact the postheat treatment of microstructure and optical property transitions. As Pb is known to destabilize the glass toward crystallization, Figure 4b illustrates the impact of morphology on refractive index after nucleation and growth [N+G] treatment. The overall increase in the glass' effective refractive index is observed as compared to that of the Pb-free base glass (0 mol% PbSe), with the exception of the lowest PbSe-containing samples. It is also important to note that following the 1 h nucleation-only step at the glass transition temperature, all glasses showed an overall drop in refractive index with a magnitude inversely proportional to Pb content.<sup>[33]</sup> Since there is little change in the postnucleated glass' transmission, which will be shown later and no modification in the amorphous nature of the glass as observed by DSC or XRD following this initial heat treatment step, this change is likely due to subtle reorganization (relaxation) in the glass' network yielding a decrease in density (and thus index) from its as-quenched and annealed structure. These data are compared to a calculated effective index for the GC approximated using a rule of mixtures,  $n_{GC} \approx V_{\text{Glass}} \times n_{\text{Glass}} + \sum_{i=1}^N (V_{\text{ith Crystal}} \times n_{\text{ith Crystal}})$  where

the volume fractions of each crystal phase ( $V_{\text{ith Crystal}}$ ) defined by XRD and the refractive index ( $n_{\text{ith Crystal}}$ ) of each crystal along with the volume fraction of glass ( $V_{\text{Glass}}$ ) and the parent glass' initial refractive index ( $n_{\text{Glass}}$ ) are considered. Note that the true residual glass' index has not been used in the calculation. This quantity, which cannot be experimentally measured, represents a known error in the approximation since the depletion of the crystal-forming species from the initial parent glass will modify (reduce in this case) the residual glass' index following crystallite formation. A discussion on the approximation offered through this equation has been previously reported in greater detail for this system.<sup>[33]</sup>

Higher Pb-containing materials possess a larger number of larger (Pb) ions and thus these glasses have a corresponding higher density and smaller molar volume. This results in the decreasing molar volume with increasing PbSe as seen in Figure 4c. Upon heat treatment, the regions with Pb in the matrix (where crystallization of a higher density phase is larger) give rise to a larger decrease in molar volume, illustrating the impact of the microstructural changes on the glass' network variation. The trend in index change seen for the nucleated-only glass is likely due to the structural role of the large Pb ion in the glass network. While the Pb is segregated in droplets beyond a

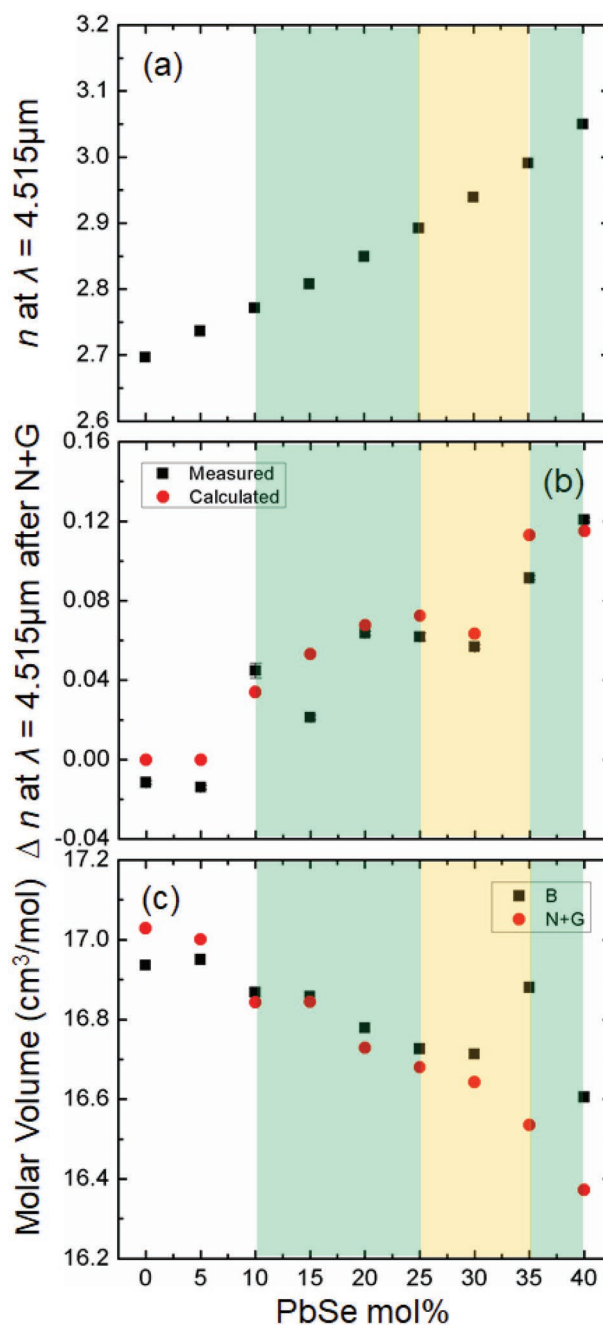


**Figure 4.** a) The base glass refractive index measured at  $\lambda = 4.515 \mu\text{m}$  as a function of PbSe content. b) The change in refractive index following a nucleation and growth [N+G] heat treatment. Calculated data points represent an average effective refractive index based on volume fraction of each crystal species and its respective refractive index, and that of the remaining fraction of the parent glass. c) Molar volume for the base (B) and nucleated and grown [N+G] samples. Coloration in background illustrates the composition regions where transition from droplet/matrix morphology (green) to spinodal morphology (yellow) occurs. The size of error bars is smaller than the size of data points in all cases ( $<0.0015$ )

level of  $\approx 10$  mol% PbSe, its structural role acts to open the glass network (as Pb can act as a modifier); at higher levels (where it transitions to a role as a matrix species beyond a level of

≈35 mol% PbSe), it is believed that Pb transitions to a role as an intermediate, possibly becoming an integral part of the glass' backbone. Such a change in structural role for Pb has been observed previously in high Pb-containing oxide glasses.<sup>[34]</sup> This interpretation supports evolutionary trends seen in other physical properties where the addition of Pb results in a concurrent increase in density and index as well as changes in  $T_g$ .<sup>[25]</sup> Lower Pb-containing glasses are also believed to possess more three-coordinated As, as compared to four-coordinated Ge or Pb; this lower constraint within the network may lead to the postnucleation index drop. In other studies of Ge–As–Se glasses, the lower Ge-containing glasses incurred a refractive index drop upon heat treatment during molding processing.<sup>[35]</sup>

The trends in the experimental data can be directly correlated with crystal phases present and their type. Pb-containing crystallites such as  $\text{Ge}_{0.1}\text{Pb}_{0.9}\text{Se}$  and PbSe generated within resulting GCs upon heat treatment have refractive indices of ≈4 which are far greater than that of base glasses which range from ≈2.70 to ≈3.05. The amount of these high refractive index Pb-containing crystallites, which can form, increases as the level of Pb present in the parent base glasses increases. Therefore,  $\Delta n$ , which is the difference in the refractive indices of a resulting glass–ceramic nanocomposite and the respective starting glass, increases with the molar percentage of PbSe. Specifically, recall glasses with 0 and 5 mol% PbSe show no evidence of crystallization upon heat treatment via XRD, indicating no formation of any crystal phase. For postheat treatment GCs with 10–30 mol% PbSe, an increase in the measured refractive index of the nanocomposite occurs and appears to remain nominally constant for GCs with 20–30 mol% PbSe. This plateau is in agreement with the data from XRD analysis which shows the total volume fraction of crystals is nearly equivalent as shown in Table 1 despite the types of crystals being slightly different. As Table 1 illustrates, the post-heat-treated GC with 10 mol% PbSe has a smaller volume fraction of the higher index  $\text{Ge}_{0.1}\text{Pb}_{0.9}\text{Se}_{1.0}$  crystals as compared to the GCs with 20–30 mol% PbSe, which causes its index to be slightly lower despite having the same volume fraction of “total” crystallization. The drop in refractive index for a GC with 15 mol% PbSe is likely due to the total volume fraction of crystal being the lowest observed (other than the glass with no crystallization), perhaps imparted by an experimental error in the measurement of index for this sample, as the heat treatment clearly generates phase formation as shown by the calculated index. This compositional region is also where the base glass' morphology transitions from Pb-rich droplets to a Pb-rich matrix with a small spinodal region. Beyond a level of 30 mol% PbSe, there is a continual increase in refractive index that tracks the increase in both Pb content and Pb-containing crystal phases. This increase also tracks with an increase in the total volume fraction of crystals present in the glass. The overlay in data in Figure 4b compares the experimentally determined indices to those calculated using the approximation of GC's index ( $n_{GC}$ ) described above. The calculated index shows a similar trend as the measured index, but as can be seen in almost all cases, the calculated index overestimates the experimentally measured index. This is likely due to assumptions made in our estimation, including that the refractive index of the remaining (depleted) glassy phase is not modified after precipitation of crystals from it; additionally, the presence of crystallite clusters

(rather than discrete, discernable single-phase crystallites) prevents our clear identification of individual sizes of crystals and therefore introduces errors in precise determination of their respective volume fractions. Both of these issues are likely the primary contributors to the observed offset. XEDS enables mapping of composition; however, the technique's spatial resolution is insufficient to precisely quantify the residual glass' depleted composition or index. However, it should be noted that a similar early indication of “nucleation” is also observed in the spatial, compositional modification seen in initially homogeneous, laser-nucleated glass films.<sup>[21]</sup> The fact that the measured and calculated indices trend together strongly indicates that the refractive index increase is dominated from the formation of crystallites in the glassy network and the concurrent decrease in the refractive index of the crystal phases' constituents in the residual glass matrix. Further efforts to quantify these subtleties are ongoing.

While absolute index change is important in consideration of use for GRIN applications, optical designers typically rely on a material's dispersion over the target spectral window of use. Refractive indices for the base GAP-Se glasses and GC materials were measured at six wavelengths across the IR spectral range at wavelengths of 1.88, 3.3, 4.515, 7.968, 9.294, and 10.717  $\mu\text{m}$ , and measured indices were subsequently fitted with a Sellmeier function  $\left( n = \sqrt{A + \frac{B\lambda^2}{\lambda^2 - C^2} + \frac{D\lambda^2}{\lambda^2 - E^2}} \right)$  and its coefficients of  $A$ ,  $B$ ,  $C$ ,  $D$ , and  $E$  were determined.<sup>[31,36]</sup> These data are shown in Figure 5a,b. With the Sellmeier coefficients for both base and heat-treated samples in all composition domains studied, Abbe numbers in the short-wave IR (SWIR)  $\left( \frac{n_{2.0\mu\text{m}} - 1}{n_{1.6\mu\text{m}} - n_{2.4\mu\text{m}}} \right)$ , MWIR  $\left( \frac{n_{4\mu\text{m}} - 1}{n_{3\mu\text{m}} - n_{5\mu\text{m}}} \right)$ , and long-wave IR (LWIR)  $\left( \frac{n_{10\mu\text{m}} - 1}{n_{8\mu\text{m}} - n_{12\mu\text{m}}} \right)$  were then extracted<sup>[17,31,37]</sup> and plotted as a function of PbSe mol%, as shown in Figure 5c. In Figure 5c, the Abbe number is shown to decrease with PbSe addition up to a level of ≈25–30 mol% PbSe. More importantly, we observe in Figure 5c that the Abbe number is dramatically impacted (reduced) when the Pb is present as a dominant species in the parent glass' matrix. This is evident in the higher dispersion of glasses dominated by a Pb-rich matrix. The dispersion in all glasses further decreases upon heat treatment and is most impacted by the types of crystals formed and their (respective) dispersive behavior. A similar trend in higher Pb-content GAP-Se films (40 mol% PbSe) was also observed following laser-induced nucleation and subsequent heat treatment.<sup>[17]</sup> In the present bulk glasses, there is a minimum in the Abbe numbers for both glass and GCs with ≈25–30 mol% PbSe, which once again is likely due to the transition in morphology in this region with the glass' Pb being present in Pb-rich droplets below ≈25 mol% PbSe changing to Pb within a Pb-rich matrix above 30 mol% PbSe.

The Pb-content variation in the GAP-Se glass series provides a range of Abbe numbers for the optical designer to choose from for chromatic correction. In the paraxial regime, the axial chromatic aberration is mitigated with a doublet when the magnitude of the Abbe number difference between the two lenses is maximized. An achromatic doublet could be replaced by a singlet with the addition of a GRIN component, as suggested in ref. [38]. The larger the magnitude of the separation between the

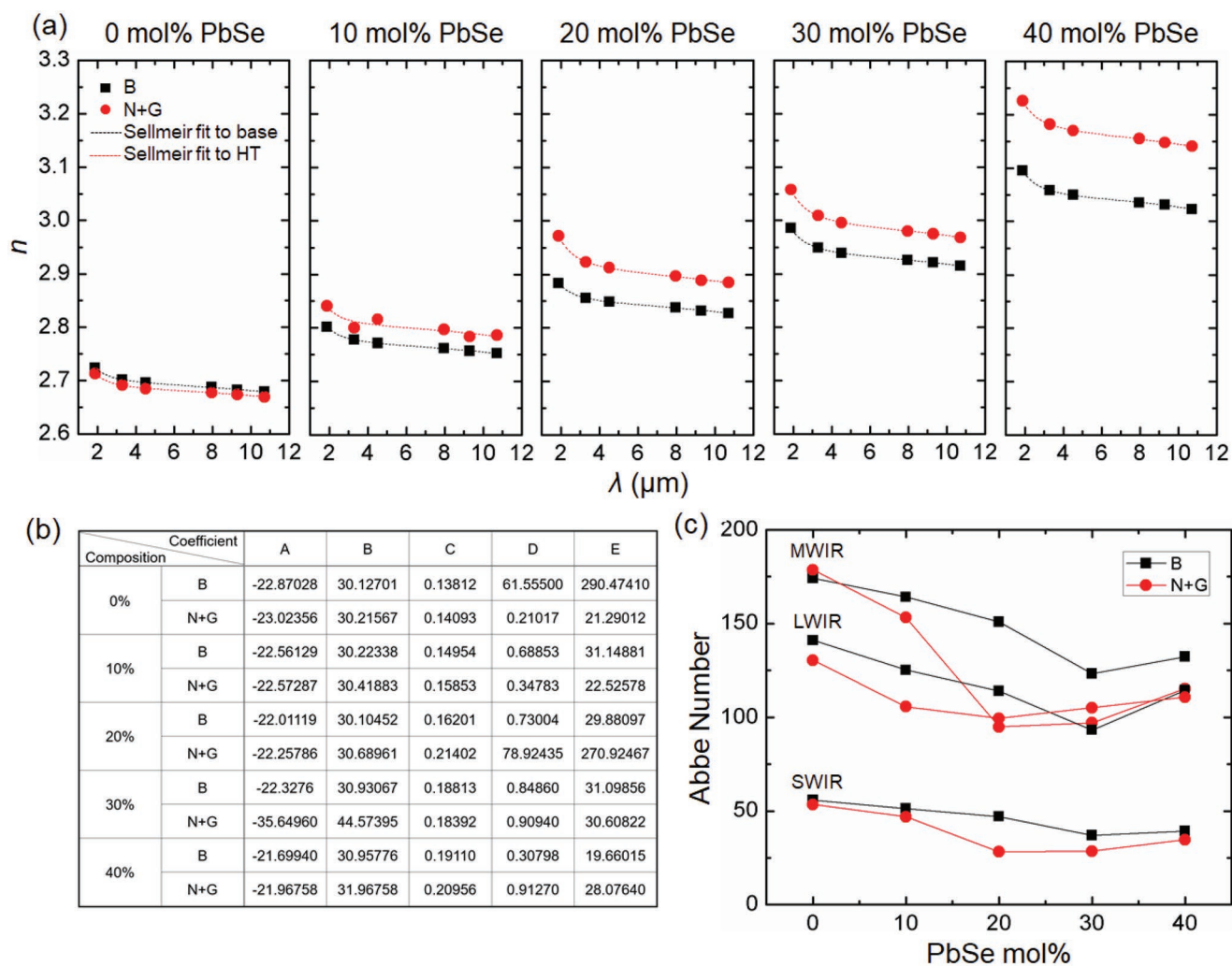


**Figure 5.** a) Multiwavelength refractive index dispersion for base (B) and nucleated and grown [N+G] samples of GAP-Se glass prior to and following nucleation and growth. Compositional evolution across 0–40 mol% PbSe series, fit to a Sellmeier function  $\left( n = \sqrt{A + \frac{B\lambda^2}{\lambda^2 - C^2} + \frac{D\lambda^2}{\lambda^2 - E^2}} \right)$ . b) Sellmeier coefficients of A, B, C, D, and E extracted from the fitted curves. c) Abbe numbers in the SWIR  $\left( \frac{n_{2.0\mu\text{m}} - 1}{n_{1.6\mu\text{m}} - n_{2.4\mu\text{m}}} \right)$ , MWIR  $\left( \frac{n_{4\mu\text{m}} - 1}{n_{3\mu\text{m}} - n_{5\mu\text{m}}} \right)$ , and LWIR  $\left( \frac{n_{10\mu\text{m}} - 1}{n_{8\mu\text{m}} - n_{12\mu\text{m}}} \right)$  calculated using the Sellmeier coefficients for base glass (B) and GC following the defined two-step nucleation and growth [N+G] protocol.

Abbe number of the base glass and the GRIN component, the larger the potential for a GRIN achromatic singlet. The Abbe number in a spectral band for the GRIN component is given by the ratio  $\frac{\Delta n_{\text{mid}}}{\Delta n_{\text{short}} - \Delta n_{\text{long}}}$ , where  $\Delta n$  is the extreme refractive index change at the short, mid, or long wavelength as indicated by the subscript (see Figure 4 for the  $\Delta n$  for each Pb-content at  $\lambda = 4.515 \mu\text{m}$ ). Figure 6 shows the refractive index versus the Abbe number for the GAP-Se bulk glasses with 0–40 mol% PbSe and their equivalent GRIN counterpart for SWIR, MWIR, and LWIR. Figure 6 also shows the same properties for other common IR materials used in achromatic doublets, specifically, silicon, germanium, ZnS, ZnSe, and BaF<sub>2</sub>. The Abbe number difference in the SWIR band between the GAP-Se with 0 mol% PbSe and its GRIN counterpart is comparable to the Abbe number difference of BaF<sub>2</sub> and ZnSe, but less than that of BaF<sub>2</sub>/Si. In the MWIR, GAP-Se with 20 mol% PbSe and

its GRIN counterpart are comparable to the combination of Si/Ge. Finally, in the LWIR, GAP-Se with 40 mol% PbSe and its GRIN counterpart is almost comparable to ZnSe/Ge or ZnS/Ge. Therefore, we confirm that GAP-Se glasses are good candidates for chromatic correction in all three bands, as defined by this single, two-step heat treatment protocol. This means that modification to the base glass value (through a change to either the nucleation and/or growth time and/or temperature) will alter the absolute position of the GC material's position on these plots. To date, we have not defined the extremes of such property tailoring (with the critical criteria that GC index and dispersion change are limited by the point where optical degradation in the form of scatter/absorption loss occurs). This sensitivity analysis is ongoing.

The impact of the precipitated crystal phase(s) in the resulting post-heat-treated GC will impact the transmission characteristics of the resulting composite. Examining the



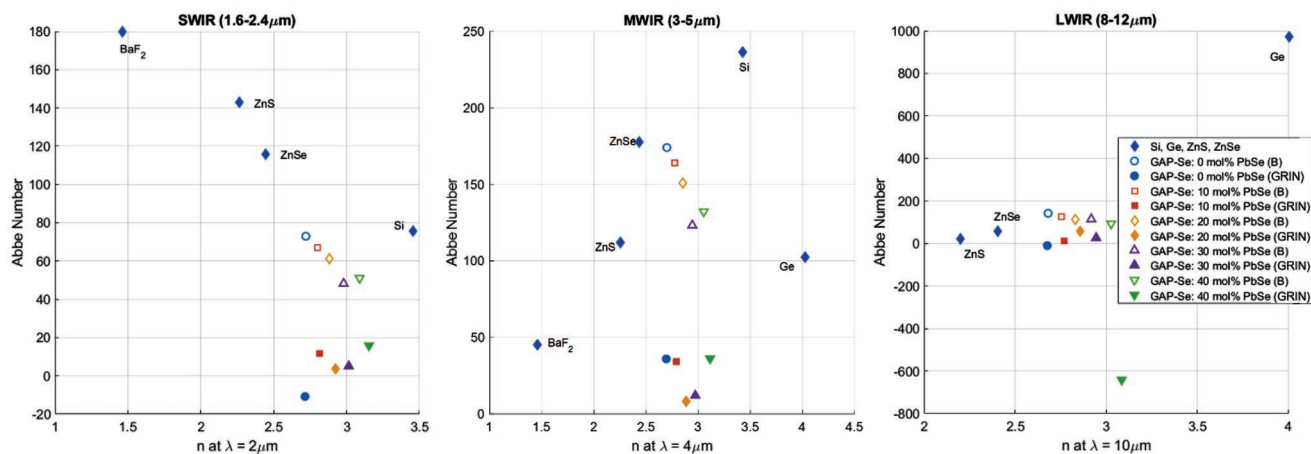


**Figure 6.** Abbe number versus the refractive index of selected IR materials and the GAP-Se glass and glass–ceramic materials at the mid-wavelength for each band: SWIR, MWIR, and LWIR. Conventional IR materials are represented by the solid blue diamonds. The GAP-Se glasses and glass–ceramics are represented by empty and solid markers, respectively. The empty markers correspond to the melt-quenched base glasses whereas the solid symbols of the same color correspond to the candidate GRIN GAP-Se glass–ceramics following the defined two-step heat treatment protocol. Recall that the Abbe number for the GRIN lens is given by  $\frac{\Delta n_{\text{mid}}}{\Delta n_{\text{short}} - \Delta n_{\text{long}}}$ , where  $\Delta n_i$  is the extreme change of refractive index at the  $i$ th wavelength. Note that the refractive index of the GRIN component is not defined necessarily by a single value. In order to compare the refractive index of each base sample and its corresponding GRIN component, the refractive index between the base and the heat-treated sample is used for the solid markers.

transmission cut-off of the parent base glass, here defined as the point of 90% of maximum transmission, one might expect to observe a minor change in position with varying PbSe mol% due to the nearly linear refractive index increase. However, we also expect that it may be affected (or dominated) by the glass' morphology. In both low and high PbSe-containing glasses, the droplet-matrix morphology would be expected to contribute to scatter loss. Similarly, while the index variation in glassy phases present in the spinodal region is likely less, the volume fraction of the secondary phase is higher in this region (spanning  $\approx 25$ – $35$  mol% PbSe). As the glass' PbSe molar percentage increases from 0% to  $\approx 25$ %, the as-melted glass' morphology evolves from homogeneous to phase separated. This can be either Pb-rich droplets in a Pb-deficient matrix or spinodal configuration.<sup>[25]</sup> This morphological variation leads to index variation in the glass phases inducing scatter loss. Hence, the size of droplets or interconnected phases will lead to a decrease in the glass' transparency, inducing a redshift of its transmission cut-off. As the percentage of PbSe increases further beyond  $\approx 25$ %, the morphology comes back to droplet-matrix configuration now with Pb-deficient droplets in a Pb-rich matrix. This change is expected to lead to an increase in its transparency as the high index glass phase now comprises the matrix, thereby reducing scatter loss and, in turn, resulting in a blueshift of the glass' transmission cut-off. The effect of these morphology differences can clearly be seen in **Figure 7a**. One can observe the emergence of a pronounced tail of the shortwave transmission edge for the glass' exhibiting phase separation region (onset just beyond 10 mol% PbSe) where the secondary phases (droplets) increase in size with increasing PbSe mol%. Beyond this composition space where spinodal decomposition begins to occur (between 25 and 30 mol% PbSe), the morphology gives rise to extensive scatter loss. The magnitude of this loss increases with heat treatment. While there is a negligible change in

the transmission cut-off position after nucleation, there is a significant change in the transmission cut-off position upon the growth of crystals, primarily due to scattering between the precipitated crystals and the residual glass, as shown in **Figure 7b**. The loss is most pronounced for mid Pb-content glasses ( $\approx 15$ – $25$  mol% PbSe) produced using the stated heat treatment protocol, where the heat-treated samples are nearly opaque. This corresponds to the growth region of large, anisotropic crystals which would be expected to have large scattering cross sections. The volume fraction of these large, anisotropic crystals stays relatively constant across all the compositions, at a level around  $13 \pm 2\%$ . For the higher Pb-content glasses (beyond 35 mol% PbSe), the content of cubic PbSe, while small in absolute quantity, becomes prominent, thereby enhancing the contribution toward the resulting effective refractive index. This results in much higher transparency across the full SWIR, MWIR, and LWIR spectral regions as shown for the GC with 40 mol% PbSe following heat treatment in **Figure 7c**. Here, the resulting nanocomposite exhibits an effective index change of  $\Delta n = +0.12$  following this specific heat treatment protocol, with transparency largely maintained. This evolution highlights the need to understand the parent glass' morphology as well as the specific crystallites that are grown and their volume fractions associated with a specific heat treatment protocol. As noted previously, the magnitude of such changes, both the index change and expected scatter loss, is a direct impact of the time and temperatures at which nucleation and growth occurs. As only one thermal protocol has been employed here, these data are thus representative of this single heat treatment protocol. Other protocols would likely impart changes in the extent of these property modifications. It is also important to note that the transmission dips at  $\approx 2.8$   $\mu\text{m}$ ,  $\approx 6$   $\mu\text{m}$ , and 8  $\mu\text{m}$  originate from impurity constituents in the glass, namely O–H, H<sub>2</sub>O, and Ge–O absorption bands, respectively.<sup>[39]</sup>

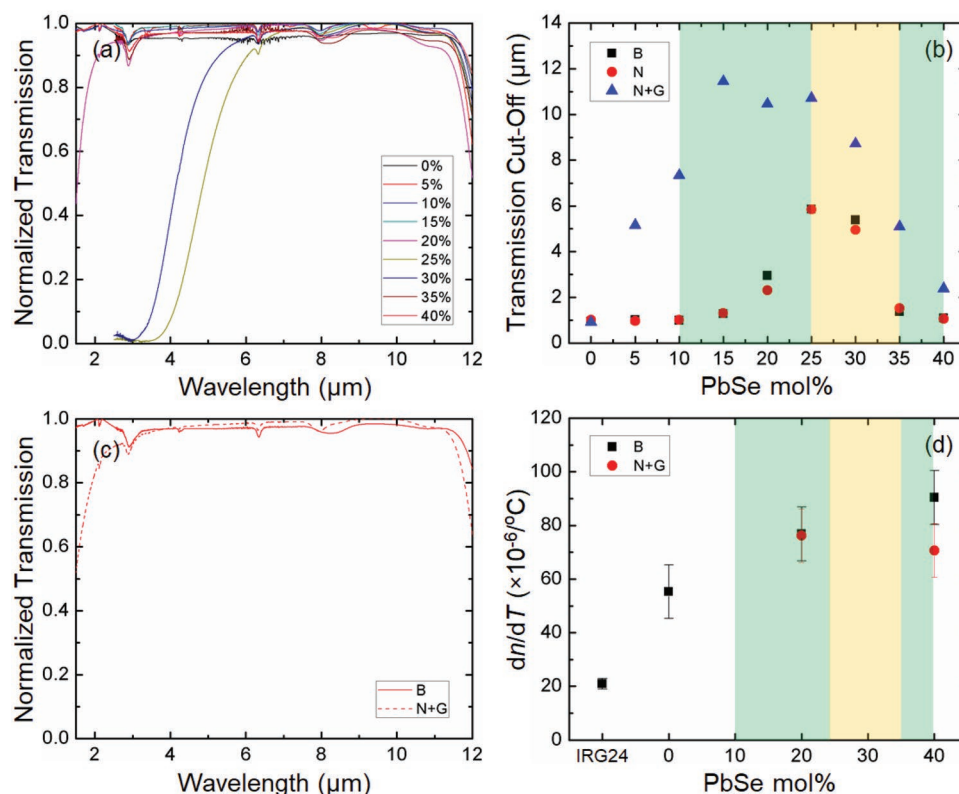


**Figure 7.** a) Normalized transmission spectra (all samples, 2 mm thick) for base glasses with PbSe mol% of 0–40% prior to heat treatment. b) The short-wave transmission cut-off ( $\mu\text{m}$ ) is shown for base [B], nucleation-only [N], and nucleated and grown [N+G] samples as a function of PbSe content. c) Normalized transmission for 2 mm thick base and post-heat-treated samples with 40 mol% PbSe. d) Values of  $dn/dT$  measured over  $\Delta T = 90^\circ\text{C}$  using the technique discussed previously<sup>[30]</sup> are shown for glasses and GCs with 0, 20, and 40 mol% PbSe.  $dn/dT$  of a commercial GeAsSe glass (SCHOTT IRG-24) over a similar temperature range is included for reference. Colorization in background illustrates transition from droplet/matrix morphology (green) to spinodal morphology (yellow).

A secondary but equally important attribute of the nanocomposite is the material's thermo-optic coefficient,  $dn/dT$ . Here,  $dn/dT$  was measured for glasses with 20 and 40 mol% PbSe in order to see the influence on this property response to temperature with the Pb species present in the droplet versus the matrix phase, as shown in Figure 7d. Added for comparison to the figure are the measured values for our 0% PbSe composition ( $\text{Ge}_{6.25}\text{As}_{37.5}\text{Se}_{56.25}$ ) as well as that of a similar commercial reference glass IRG-24 glass ( $\text{Ge}_{10}\text{As}_{40}\text{Se}_{50}$ ) manufactured by SCHOTT.<sup>[40]</sup> It should be noted that the methodology used by SCHOTT to measure  $dn/dT$  is not identical to the protocol used here, though the two methods have been compared previously.<sup>[35]</sup> As can be seen,  $dn/dT$  of the base glass increases as the amount of Pb is increased from 0 to 40 mol% PbSe. As discussed in both of these prior references, this evolution can be related to both the index and the change in thermal expansion coefficient of the respective glasses, though the latter was not explicitly measured here. After ceramization, the glass with 40 mol% PbSe exhibits a marked decrease in  $dn/dT$  and was shown to be lower than that of the glass with 20 mol% PbSe upon heat treatment. The nucleated and grown glass with 20 mol% PbSe does not exhibit a significant change in  $dn/dT$ . This difference in behavior is likely due to the difference in the crystal phases that have formed in the respective compositions

upon heat treatment. As  $dn/dT$  of the composite is dependent on the  $dn/dT$  of each crystal phase and its volume fraction as well as the depleted glassy phase's modified  $dn/dT$  following departure of crystal phase forming species, all phases will undergo changes in both index and thermal expansion upon heat treatment. It is also likely that the crystallization of Pb-rich phases contained in the matrix of the glass with 40 mol% PbSe dominates the glass–ceramic composite's resulting behavior, with its minor Pb-deficient phase (richer in lower index As–Se crystallite content) contributing less to the composite's  $dn/dT$ . These As–Se phases are in higher concentrations in the lower Pb-content composite (20 mol% PbSe), as shown in Table 1, whereas PbSe-containing crystals are fewer in the 20 mol% composition as compared to the 40 mol% medium. The attributes of these respective regions are difficult to quantify but the trends are consistent throughout.

### 3. Conclusion

In conclusion, multicomponent GAP–Se ChG glass and glass–ceramic nanocomposites have been characterized for their tailorable index, dispersion, and thermo-optic properties. The evolution of these properties as a function of PbSe content has

been related to the parent glass' morphology (phase separation), and the role of this starting composition on the resulting crystal phases precipitated using a defined heat treatment protocol. Optical properties of each material were measured pre- and postheat treatment to ascertain and correlate changes associated with crystal phase formation. The change in material properties following a fixed, two-step heat treatment has been directly correlated with variation in quantity of the dominant Pb-containing phases in the starting material. The type and total volume fraction of crystalline phase(s) formed upon heat treatment have been quantified, and it has been shown that the relative amounts of the formed crystals are dependent on the starting composition of the parent glass. Effective refractive indices of the composites have been measured in the mid-wave infrared and compared to that calculated based on an effective medium approximation considering crystal type, volume fraction, and depleted medium refractive index. The close correlation of these data provides an excellent assessment of the material's post-heat treatment modification and the resulting optical transmission, refractive index, and dispersion modification. Lastly, the use of this fixed, two-step heat treatment results in dramatic variations in Abbe number and material dispersion. The variation in dispersion has been characterized in the near-, mid-, and longwave infrared regions and is shown to vary with Pb-content and the dominant phase within which the Pb resides. While the pre- and postheat treatment optical properties exhibit a minima in Abbe number near the spinodal region of morphology transition in each spectral region, the slope of the changes varies significantly offering design options within each of the spectral regions. The broadband index and dispersion attributes of the base glass and nanocomposites have been compared with existing infrared optical materials and have been shown to provide attributes that lend themselves to use as color correction pairs in conventional optical designs. This suggests that the large variation in Abbe number demonstrated for this singular heat treatment protocol can be exploited to enhance design strategies for specific applications through the use of such optical nanocomposite materials. Furthermore, our material and process can be applied to a wide variety of integrated optical systems (bulk or film) where specific refractive indices are needed to realize specific optical function of components. For example, index matching materials in fiber optics and antireflecting layers with specific indices are expected to be greatly benefited by our novel technique.

#### 4. Experimental Section

**Glass Fabrication:** Bulk glass GAP-Se glasses with compositions of  $(\text{GeSe}_2-3\text{As}_2\text{Se}_3)_{1-x}\text{PbSe}_x$ , with  $x = 0-40$  mol% in 5 mol% increments, were melted and quenched from elemental starting materials in small 40 g batches.<sup>[23,25]</sup> The resulting 10 mm diameter rods of glass were then annealed and sliced into  $\approx 2$  mm thick disks. These disks were then double-sided polished with a PR Hoffman double-sided lapping machine (PR-2) with a 5  $\mu\text{m}$  slurry. Final surfaces were hand-polished with a 0.05  $\mu\text{m}$  slurry, resulting in a nominal  $18 \pm 6$  nm surface roughness.

**Heat Treatments:** Heat treatment steps were carried out in a muffle furnace (ThermoScientific 48000) in air atmosphere calibrated with a type K thermocouple that was placed next to the samples on the same refractory brick. In order to systematically determine a nucleation and

growth heat treatment protocol for the varying glass compositions with limited prior knowledge of the nucleation and growth behavior for each, the nucleation temperature was set to be the glass transition temperature of each glass type and the growth temperature was set to the peak of the first crystallization peak of each glass type as determined by a DSC (Netzsch DSC 204 F1 Phoenix) and are shown in the Supporting Information.<sup>[23]</sup> Subsequent studies have further quantified precise nucleation- and growth-like curves for glasses with 20 and 40 mol% PbSe, and these data are likewise included in the supplemental information.<sup>[23]</sup> In the present study, the heat treatment times were constant, with nucleation steps performed for an hour and growth steps for 30 min. Samples were isothermally treated by placing them inside the furnace after the furnace was at the targeted temperature for nominally 30 min.

**XRD Experiments:** XRD was performed using a PANalytical Empyrean, basic X-ray diffraction system with a beam power of 1.8 kW, a beam wavelength of  $\lambda_{\text{Cu}_K\alpha} = 0.15418$  nm, and a beam current of 40 mA at room temperature. XRD measurements were performed on one base and one nucleated and grown sample for each composition in order to confirm that the base glass was amorphous and to identify crystal phases that formed upon heat treatment. The XRD spectra were fitted with peaks from crystals identified using SAED data collected from samples with 20 and 40 mol% PbSe which underwent similar heat treatment.<sup>[23]</sup> The volume fractions of the different crystal phases present were also measured based on the intensities of the crystal peaks. A correction factor was found to not be necessary to account for Pb shielding from the remaining glassy matrix by adding in known quantities of crystalline PbSe to 0 and 40 mol% PbSe.

**Electron Microscopy:** TEM was performed on heat-treated glasses with 20 and 40 mol% PbSe. The images were obtained using 80–200 keV voltage, 1 nA current, and 57–225k magnification. SAED was performed on the heat-treated glasses to confirm crystallinity and identify the types of crystals from the electron diffraction pattern. Cross-sectional TEM samples were prepared by using a focused ion beam-assisted milling followed by a lift-out process. This process was conducted using the FEI Helios 660 dual-beam with carbon and Pt gas injection system (GIS). XEDS was performed on the TEM samples to assess how the elements are segregated in the glass.

**Refractive Index Measurements:** The refractive index was measured on a Metricon prism coupler that was modified for use in the IR.<sup>[41–44]</sup> For each composition, room-temperature index measurements were conducted on base and postheat-treated samples at six wavelengths across the IR including 1.88, 3.3, 4.515, 7.968, 9.294, and 10.717  $\mu\text{m}$ . The experimental uncertainty of the measurement was typically on the order of  $10^{-4}$  refractive index units (RIU); however, can be better in high quality, large melt specimens. Such sources of the uncertainty are attributable to the spatial compositional and density variations more prominent in small melt sizes, as well as inhomogeneous surface topography of the test specimen. The indices were fitted with

a Sellmeier curve  $\left( n = \sqrt{A + \frac{B\lambda^2}{\lambda^2 - C^2} + \frac{D\lambda^2}{\lambda^2 - E^2}} \right)$  and SWIR  $\left( \frac{n_{2.0\mu\text{m}} - 1}{n_{1.6\mu\text{m}} - n_{2.4\mu\text{m}}} \right)$ , MWIR  $\left( \frac{n_{4\mu\text{m}} - 1}{n_{3\mu\text{m}} - n_{5\mu\text{m}}} \right)$ , and LWIR  $\left( \frac{n_{10\mu\text{m}} - 1}{n_{8\mu\text{m}} - n_{12\mu\text{m}}} \right)$  and Abbe numbers were

then extracted from the fitted curves.<sup>[17,31,36,37]</sup>  $dn/dT$ , the thermo-optic coefficient, was measured at 4.515  $\mu\text{m}$  at temperatures of 30, 50, 70, and 90 °C and repeated in similar 20 °C steps from 90 to 30 °C. Appropriate thermal holds were carried out at each step temperature. This thermal protocol was carried out to ensure that there is no relaxation of the glass at 90 °C that would alter the index upon cooling from the higher temperature. A best-fit line of the data was used to calculate the  $dn/dT$ . The error for this calculation is generally 10 ppm. Additionally, the same  $dn/dT$  measurement protocol was employed on commercial reference glasses to validate the reliability of this protocol. These commercial glasses have their own published thermo-optic  $dn/dT$  values, measured with a commercial analysis method that does not employ an identical protocol used in this study.<sup>[35]</sup> This results in an identical slope of the  $dn/dT$  best fit line, but a vertical offset of the absolute index values.

**Molar Volume:** Molar volume was calculated by dividing the molar mass of each glass by its measured density at room temperature. Density measurements were conducted within an immersion fluid of deionized water at room temperature using an AE Adams PGW Balance.

**Calculated Effective Refractive Index:** XRD data were used to quantify the volume fractions of the different crystals present, along with measured 4.515  $\mu\text{m}$  refractive index values of the crystals; these values include  $\text{Ge}_{0.1}\text{Pb}_{0.9}\text{Se}_{1.0} = 4.5$ ,  $\text{PbSe} = 4.9$ ,  $\text{As}_2\text{Se}_3 = 2.7$ , and  $\text{Se} = 2.79^{[45-47]}$  to calculate the effective refractive index of the samples by multiplying the volume fraction of each phase with its index and then adding this value for the various phases identified via XRD. The index of the residual glassy phase was not adjusted for Pb, As, Ge, or As departure to form the crystalline species created, rather was held at the refractive index of the base glass for each composition. Volume fraction of glass was therefore determined to be 100% less the total fraction crystallized.

**Transmission Measurements:** Each glass' transmission window was quantified for the base, nucleation-only, and nucleated and grown samples. Transmission measurements were made using a CARY 500 UV-VIS spectrophotometer or a ThermoFisher Nicolet iS5 FTIR, depending on the samples' optical transmission cut-off. As the true transmission cut-off is very difficult to measure accurately for bulk glasses, here it is defined as a wavelength corresponding to 90% of the maximum transmission.<sup>[48]</sup>

## Supporting Information

Supporting Information is available from the Wiley Online Library or from the author.

## Acknowledgements

L.S. and M.K. contributed equally to this work. This work was supported by the Defense Advanced Research Projects Agency under Air Force Research Laboratory contract FA8650-12-C-7225 through the M-GRIN Tech Area 2 program. The views, opinions, and/or findings expressed are those of the author and should not be interpreted as representing the official views or policies of the Department of Defense or the U.S. Government. The authors acknowledge the helpful insight from discussions with Prof. Edgar Zanotto and Prof. Carlo Pantano as well as Dr. Alexej Pogrebnaykov related to the goals of this work.

## Conflict of Interest

The authors declare no conflict of interest.

## Keywords

chalcogenide glass, glass-ceramics, gradient refractive index, GRIN dispersion engineering, optical nanocomposites

Received: March 17, 2019

Revised: May 31, 2019

Published online: June 24, 2019

[1] FLIR ONE Thermal Imaging Camera, <http://www.flir.com/flirone/ios-android/> (accessed: March 2019).

[2] L. Calvez, H. Ma, J. Lucas, X. Zhang, *Adv. Mater.* **2007**, *19*, 129.

- [3] Thermal Imaging Cameras for Machine Vision/Industrial Safety, <http://www.flir.com/automation/content/?id=65833> (accessed: March 2019).
- [4] C. Lin, L. Calvez, M. Roze, H. Tao, X. Zhang, X. Zhao, *Appl. Phys. A* **2009**, *97*, 713.
- [5] L. Calvez, H. L. Ma, J. Lucas, X. H. Zhang, *J. Non-Cryst. Solids* **2008**, *354*, 1123.
- [6] X. Zhang, M. A. Hongli, J. Lucas, *J. Non-Cryst. Solids* **2004**, *337*, 130.
- [7] S. D. Campbell, D. E. Brocker, J. Nagar, D. H. Werner, *Appl. Opt.* **2016**, *55*, 3594.
- [8] K. Richardson, M. Kang, L. Siskin, A. Yadav, C. Blanco, M. Antia, S. Novak, B. Gleason, C. Smith, A. Buff, A. Lepicard, M. Dussauze, C. Schwarz, S. Kuebler, C. Grabill, C. Pantano, T. Mayer, A. Pogrebnaykov, C. Rivero-Baleine, A. Kirk, S. Mensah, M. Driggers, J. Hu, P.-T. Lin, A. Agarwal, C. Li, W. Deng, *Proc. SPIE* **2018**, *10627*, 106270A.
- [9] G. Beadie, E. Fleet, J. S. Shirk, in *Frontiers in Optics 2010*, Optical Society of America, New York **2010**, FThU5.
- [10] G. Beadie, J. S. Shirk, A. Rosenberg, P. A. Lane, E. Fleet, A. R. Kamdar, Y. Jin, M. Ponting, T. Kazmierczak, Y. Yang, A. Hiltner, E. Baer, *Opt. Express* **2008**, *16*, 11847.
- [11] Y. Jin, H. Tai, A. Hiltner, E. Baer, J. S. Shirk, *J. Appl. Polym. Sci.* **2007**, *103*, 1834.
- [12] M. A. Pickering, R. L. Taylor, D. T. Moore, *Appl. Opt.* **1986**, *25*, 3364.
- [13] J. Hunt, T. Tyler, S. Dhar, Y. Tsai, P. Bowen, S. Larouche, N. M. Jokerst, D. R. Smith, *Opt. Express* **2012**, *20*, 1706.
- [14] C. M. Schwarz, C. N. Grabill, G. D. Richardson, S. Labh, A. M. Lewis, A. Vyas, B. Gleason, C. Rivero-Baleine, K. Richardson, A. Pogrebnaykov, T. S. Mayer, C. Drake, S. M. Kuebler, *J. Micro/Nanolithogr., MEMS, MOEMS* **2017**, *16*, 023508.
- [15] S. Novak, P. T. Lin, C. Li, C. Lumdee, J. Hu, A. Agarwal, P. G. Kik, W. Deng, K. Richardson, *ACS Appl. Mater. Interfaces* **2017**, *9*, 26990.
- [16] R. Buczynski, A. Anuszkiewicz, P. Stafiej, J. Lisowska, A. Filipkowski, D. Pysz, J. Cimek, M. Trippenbach, R. Kasztelanica, *Proc. SPIE* **2018**, *10712*, 1071216.
- [17] M. Kang, A. M. Swisher, A. V. Pogrebnaykov, L. Liu, A. Kirk, S. Aiken, L. Siskin, C. Lonergan, J. Cook, T. Malendevych, F. Kompan, I. Divliansky, L. B. Glebov, M. C. Richardson, C. Rivero-Baleine, C. G. Pantano, T. S. Mayer, K. Richardson, *Adv. Mater.* **2018**, *30*, 1803628.
- [18] M. Kang, L. Siskin, J. Cook, C. Blanco, M. C. Richardson, I. Mingareev, K. Richardson, *Opt. Mater. Express* **2018**, *8*, 2722.
- [19] M. Dussauze, A. Lepicard, F. Bondu, V. Rodriguez, F. Adamietz, T. Cardinal, E. Fargin, K. Richardson, *European Patent Application #EP16176689.4*, **2016**.
- [20] A. Lepicard, F. Bondu, M. Kang, L. Siskin, A. Yadav, F. Adamietz, V. Rodriguez, K. Richardson, M. Dussauze, *Sci. Rep.* **2018**, *8*, 7388.
- [21] A. Lepicard, F. Adamietz, V. Rodriguez, K. Richardson, M. Dussauze, *Opt. Mater. Express* **2018**, *8*, 1613.
- [22] L. Siskin, C. Smith, A. Buff, M. Kang, K. Chamma, P. Wachtel, J. D. Musgraves, C. Rivero-Baleine, A. Kirk, M. Kalinowski, M. Melvin, T. Mayer, K. Richardson, *Opt. Mater. Express* **2017**, *7*, 3077.
- [23] A. K. Buff, *Master's thesis*, Department of Materials Science and Engineering, University of Central Florida **2016**.
- [24] G. Yang, X. Zhang, J. Ren, Y. Yunxia, G. Chen, *J. Am. Ceram. Soc.* **2007**, *90*, 1500.
- [25] A. Yadav, M. Kang, C. Smith, J. Lonergan, A. Buff, L. Siskin, K. Chama, C. Blanco, J. Caraccio, T. Mayer, C. Rivero-Baleine, K. Richardson, *Phys. Chem. Glasses: Eur. J. Glass Sci. Technol., Part B* **2017**, *58*, 115.
- [26] A. Yadav, A. Buff, M. Kang, L. Siskin, C. Smith, J. Lonergan, C. Blanco, M. Antia, M. Driggers, A. Kirk, C. Rivero-Baleine, T. Mayer, A. Swisher, A. Pogrebnaykov, A. R. Hilton Jr., G. Whaley, T. J. Loretz, A. Yee, G. Schmidt, D. T. Moore, K. Richardson, *Int. J. Appl. Glass Sci.* **2019**, *10*, 27.

- [27] C. Liu, G. Tang, L. Luo, W. Chen, *J. Am. Ceram. Soc.* **2009**, 92, 245.
- [28] I. D. Aggarwal, C. T. Moynihan, P. B. Macedo, J. J. Mecholsky, G. R. Srinivasan, *J. Am. Ceram. Soc.* **1972**, 55, 366.
- [29] C. T. Moynihan, P. B. Macedo, I. D. Aggarwal, U. E. Schnaus, *J. Non-Cryst. Solids* **1971**, 6, 322.
- [30] J. J. Mecholsky, C. T. Moynihan, P. B. Macedo, G. R. Srinivasan, *J. Mater. Sci.* **1976**, 11, 1952.
- [31] C. Goncalves, M. Kang, B.-U. Sohn, G. Yin, J. Hu, D. T. H. Tan, K. Richardson, *Appl. Sci.* **2018**, 8, 2082.
- [32] K. Richardson, A. Buff, C. Smith, L. Siskin, J. D. Musgraves, P. Wachtel, T. Mayer, A. Swisher, A. Pogrebnyakov, M. Kang, C. Pantano, D. Werner, A. Kirk, S. Aiken, C. Rivero-Baleine, *Proc. SPIE* **2016**, 9822, 982205.
- [33] L. Siskin, *Ph.D. Dissertation*, College of Optics and Photonics, University of Central Florida **2017**.
- [34] J. McKinley, *Master Dissertation*, Department of Mechanical, Materials and Aerospace Engineering (MMAE), University of Central Florida **1996**.
- [35] B. Gleason, *Ph.D. Dissertation*, Department of Materials Science and Engineering, Clemson University **2015**.
- [36] G. Ghosh, *Appl. Opt.* **1997**, 36, 1540.
- [37] D. Gibson, S. Bayya, V. Nguyen, J. Sanghera, M. Kotov, G. Drake, *Proc. SPIE* **2015**, 9451, 94511P.
- [38] J. Corsetti, P. McCarthy, D. Duncan, *Opt. Eng.* **2013**, 52, 112109.
- [39] D. S. Ma, P. S. Danielson, C. T. Moynihan, *J. Non-Cryst. Solids* **1980**, 37, 181.
- [40] Schott Advanced Optics, [https://www.schott.com/d/advanced\\_optics/f8f8c655-521a-4404-b0fa-42b678dbfe8c/1.6/schott-infrared-chalcogenide-glasses-irg-24-english-10042017.pdf](https://www.schott.com/d/advanced_optics/f8f8c655-521a-4404-b0fa-42b678dbfe8c/1.6/schott-infrared-chalcogenide-glasses-irg-24-english-10042017.pdf) (accessed: March 2019).
- [41] N. C. Anheier, H. A. Qiao, *Proc. SPIE* **2011**, 8016, 80160E.
- [42] N. Carlie, N. C. Anheier, H. A. Qiao, B. Bernacki, M. C. Phillips, L. Petit, J. D. Musgraves, K. Richardson, *Rev. Sci. Instrum.* **2011**, 82, 053103.
- [43] H. A. Qiao, K. A. Lipschultz, N. C. Anheier, J. S. McCloy, *Opt. Lett.* **2012**, 37, 1403.
- [44] B. Gleason, K. Richardson, L. Siskin, C. Smith, *Int. J. Appl. Glass Sci.* **2016**, 7, 374.
- [45] J. N. Zemel, J. D. Jensen, R. B. Schoolar, *Phys. Rev.* **1965**, 140, A330.
- [46] A. Zakery, S. R. Elliott, *Optical Nonlinearities in Chalcogenide Glasses and Their Applications*, Springer, Berlin **2007**.
- [47] L. Gampel, F. M. Johnson, *J. Opt. Soc. Am.* **1969**, 59, 72.
- [48] A. Prasad, C. Zha, R. Wang, A. Smith, S. Madden, B. Luther-Davies, *Opt. Express* **2008**, 16, 2804.